HHS Public Access

Author manuscript

J Neurochem. Author manuscript; available in PMC 2019 March 25.

Published in final edited form as:

J Neurochem. 2018 March ; 144(6): 791–804. doi:10.1111/jnc.14291.

Kinetic modeling of [^{18}F]VAT, a novel radioligand for PET imaging vesicular acetylcholine transporter (VAChT) in nonhuman primate brain

Hongjun Jin[1], **Xuyi Yue**[1], **Hui Liu**[1], **Junbin Han**[1], **Hubert Flores**[2], **Yi Su**[1,2], **Stanley M. Parsons**[3], **Joel S. Perlmutter**[1,2,4], and **Zhude Tu**[1,*]

[1]Department of Radiology, Washington University School of Medicine, St. Louis, MO 63110, USA

[2]Department of Neurology, Washington University School of Medicine, St. Louis, MO 63110, USA

[3]Department of Chemistry and Biochemistry, University of California, Santa Barbara, CA 93106, USA

[4]Department of Neuroscience, Physical Therapy and Occupational Therapy, Washington University School of Medicine, St. Louis, MO 63110, USA

Abstract

Molecular imaging of vesicular acetylcholine transporter (VAChT) in the brain provides an important cholinergic biomarker for the pathophysiology and treatment of dementias including Alzheimer's disease (AD). In this study, kinetics modeling methods were applied and compared for quantifying regional brain uptake of the VAChT-specific PET radiotracer, ((-)-(1-(-8-(2-fluoroethoxy)-3-hydroxy-1,2,3,4-tetrahydronaphthalen-2-yl)piperidin-4-yl)(4-fluorophenyl)-methanone) ([^{18}F]VAT) in macaques. Total volume distribution (V_T) estimates were compared for one-tissue compartment model (1TCM), two-tissue compartment model (2TCM), Logan graphic analysis (LoganAIF) and multiple linear analysis (MA1) with arterial blood input function using data from three macaques. Using the cerebellum-hemispheres as the reference region with data from seven macaques, three additional models were compared: reference tissue model (RTM), simplified reference tissue model (SRTM), and Logan graphic analysis (LoganREF). Model selection criterion (MSC) indicated that a) 2TCM and SRTM were the most appropriate kinetics models for [^{18}F]VAT; and b) SRTM was strongly correlated with 2TCM (Pearson's coefficients $r > 0.93$, $p < 0.05$). Test-retest studies demonstrated that [^{18}F]VAT has good reproducibility and reliability (TRV < 10%, ICC > 0.72). These studies demonstrate [^{18}F]VAT is a promising VAChT PET tracer for quantitative assessment of VAChT levels in the brain of living subjects.

*Corresponding author: Zhude Tu, Ph.D., Department of Radiology, Washington University School of Medicine, 510 South Kingshighway Blvd., St. Louis, MO 63110, USA, Tel.: +1-314-362-8487; Fax: +1-314-362-8555; tuz@mir.wustl.edu.
DR. ZHUDE TU (Orcid ID : 0000-0003-0325-835X)

Declaration of conflicting interests

The author(s) declared no potential conflicts of interest with respect to the research, authorship, and/or publication of this article.

Authors' contributions

HJ and ZT contributed significantly to the overall work design. HJ, XY, HL and JH provided the arterial blood input data. HJ, YS and HF provided the PET data that were then analyzed by HJ and YS. XY and JH contributed to radiochemistry data interpretation. HJ prepared the manuscript with input from ZT, XY, HL, SMP and JSP.

Graphical Abstract

PET imaging of vesicular acetylcholine transporter (VAChT) in brain provides an important cholinergic biomarker for the pathophysiology and treatment of dementias including Alzheimer's disease (AD). In this study, kinetics modeling methods were applied and compared for quantifying regional brain uptake of the VAChT-specific PET radiotracer [18F]VAT in macaques. The results demonstrated that [18F]VAT is a promising VAChT PET tracer for quantitative assessment of VAChT levels in the brain of living subjects.

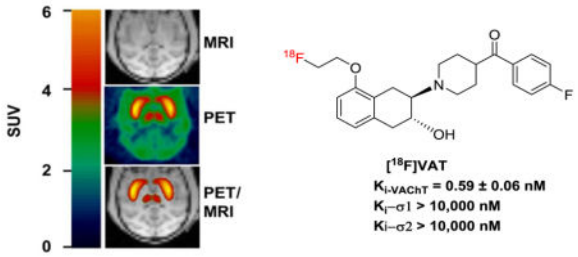

Keywords

Vesicular acetylcholine transporter (VAChT); positron emission tomography (PET); tracer kinetic modeling; [^{18}F]VAT; binding potential (BP)

Introduction

Loss of cholinergic neurons and synapses contributes to progressive cognitive dysfunction in Alzheimer's disease (AD), Parkinson disease (PD), and Huntington disease (HD) (Bohnen & Albin 2011, Braak *et al.* 2004, Pirker *et al.* 2003, Bohnen *et al.* 2003, Ransome & Hannan 2012). Vesicular acetylcholine transporter (VAChT), predominantly found in pre-synaptic terminal vesicles, is responsible for loading newly synthesized acetylcholine (ACh) from the cytoplasm into pre-synaptic vesicles. VAChT provides a reliable biomarker for cholinergic neurons under normal (Prado *et al.* 2013, Haense *et al.* 2012, Efange 2000) and neurodegenerative conditions (Bohnen & Albin 2011, Bohnen *et al.* 2009). Recent immunohistochemistry evidence found that VAChT and α-synuclein, a distinctive hallmark of PD, are co-expressed in cholinergic axons and involved in the fusion of vesicles with the presynaptic membrane (Sharrad *et al.* 2013b, Sharrad *et al.* 2013a). These studies suggest that VAChT might play a pivotal role in neurodegeneration. Concordantly, positron emission tomography (PET) imaging with a suitable VAChT-specific radiotracer that can assess the loss of cholinergic synapses or neurons would provide a useful tool for determining the severity of neurodegenerative diseases.

Vesamicol [(-)-2-(4-phenylpiperidino) cyclohexanol] was identified decades ago as a lead ligand for VAChT (Anderson *et al.* 1986). Due to its cross reactivity with $\sigma_{1/2}$ receptors in the brain, initial efforts focused on optimizing the structures of vesamicol analogues to increase selectivity for $\sigma_{1/2}$ receptors, and to improve *in vivo* kinetics and metabolic stability (Li *et al.* 2013, Tu *et al.* 2012, Wang *et al.* 2011, Tu *et al.* 2009, Kawamura *et al.* 2006, Efange 2000). The first FDA-approved VAChT radiotracer, (-)-5-[^{123}I]iodobenzovesamicol

(IBVM, (-)-*trans*-2-hydroxy-3-[4-(3-iodophenyl)piperidyl]-1,2,3,4-tetrahydrona-phthalene), was applied to assess cholinergic deficiency in patients with AD and Parkinson Disease Dementia (PDD) using single-photon emission computed tomography (SPECT), but slow binding kinetics required a scan for approximately 6 h post-injection (Mazere *et al.* 2013, Barret *et al.* 2008, Giboureau *et al.* 2007, Efange *et al.* 2000). Nishiyama et al. reported ^{11}C-labeled (*R,R)-trans*-8-methyl-2-hydroxy-3-[4-[2-aminophenyl]-piperizinyl]tetralin ([^{11}C](*R,R*)HAPT), a vesamicol derivative (Nishiyama *et al.* 2014); PET imaging studies in nonhuman primates (NHP) showed that this tracer can specifically bind to VAChT-enriched regions, and time-activity curves (TACs) of [^{11}C](*R,R*)HAPT peaked within 20 min post injection (Nishiyama et al. 2014). However it still bound to $\sigma_{1/2}$ receptors with nanomolar affinity, resulting in only 10-fold selectivity for VAChT versus $\sigma_{1/2}$ receptors (Shiba *et al.* 2006, Kawamura et al. 2006). Furthermore, the short half-life of carbon-11 (20.4 min) also obliged producing the tracer on site, which limited its applications for data acquisition at longer time periods. Koeppe and colleagues optimized the structure of IBVM to include a fluorine-18 label yielding (–)-5-[^{18}F]-fluoroethoxybenzovesamicol ([^{18}F]-FEOBV) suitable for imaging VAChT in rodents and nonhuman primates (Kilbourn *et al.* 2009, Giboureau et al. 2007, Cyr *et al.* 2014), as well as in healthy human volunteers (Petrou *et al.* 2014). PET Studies using [^{18}F]-FEOBV in rat models of cholinergic deficits and in AD patients reported decreased tracer uptake in brain regions that had cholinergic neuron terminal losses and/or related with AD pathologies (Aghourian *et al.* 2017, Cyr *et al.* 2015, Parent *et al.* 2012, Cyr et al. 2014, Parent *et al.* 2013). However, the slow kinetics required scans over 360 min for full compartmental kinetics analysis (Petrou et al. 2014, Cyr et al. 2014).

Our group has developed a new class of VAChT selective inhibitors that a carbonyl group was interposed between aromatic ring and the piperidine ring; these compounds have high affinity to VAChT with K_i values less than 10 nM, and the selectivity for VAChT versus $\sigma_{1/2}$ receptors over thousands fold (Tu *et al.* 2015, Li et al. 2013, Tu et al. 2012, Wang et al. 2011, Efange *et al.* 2010, Tu et al. 2009). We initially reported the *in vivo* specificity, and tracer kinetics of (-)-[^{11}C]TZ659 (Jin *et al.* 2016). To overcome the limitation of the short half-life of the carbon-11 isotope, we subsequently developed an F-18 labeled analogue, ((-)-(1-(-8-(2-fluoroethoxy)-3-hydroxy-1,2,3,4-tetrahydronaphthalen-2-yl)piperidin-4-yl)(4-fluoro-phenyl)-methanone) ([^{18}F]VAT) with a Ki value of 0.59 nM, and with over 10,000-fold selectivity for VAChT versus σ1/2 receptors (Tu et al. 2015). Recently we have reported automated production of [^{18}F]VAT in a Current Good Manufacturing Practice (cGMP) cyclotron facility (Yue *et al.* 2016) and the whole-body PET studies in NHPs for human dosimetry estimates (Karimi *et al.* 2015). These studies collectively suggest that [^{18}F]VAT is a promising radiopharmaceutical for imaging VAChT *in vivo* (Tu et al. 2015, Li et al. 2013, Karimi et al. 2015, Yue et al. 2016). Herein, we report the kinetics modeling of radiotracer [^{18}F]VAT in the brain of nonhuman primate. To identify optimal method for quantitative measuring the VAChT level in the brain, several kinetics modeling methods were carried out and compared for the *in vivo* quantification of the brain regional uptake of [^{18}F]VAT. The test-retest reproducibility of [^{18}F]VAT in nonhuman primates was also investigated.

Materials and methods

Radiochemistry and Chemicals

The synthesis and the radiolabeling of [^{18}F]VAT were accomplished as previously described (Yue et al. 2016, Tu et al. 2015). The radiochemical yield was 30–40% (decay corrected to end of synthesis) with a radiochemical purity > 99%, chemical purity > 95%, and mean specific activity > 63 GBq /μmol (n > 30, decay corrected to end of synthesis).

Nonhuman primate (NHP) subjects

Seven male cynomolgus macaques (NCBI_Taxon:9541, Age: 6.9 ± 0.7 years, weight: 8.0 ±1.5 kg, mean ± SD) were used for PET imaging studies, and the detail information of each macaque is summarized in Table 1. All procedures regarding the study design, animal experiments, statistical analysis, and data reporting fulfil the criteria of the Animal Research: Reporting of *In Vivo* Experiments (ARRIVE) guidelines (http://www.nc3rs.org.uk/page.asp?id=1357). Predetermined sample size were not calculated. No randomization was performed. Animals that did not complete the whole 120-minute scan or had head movement during the study were excluded. No animals were excluded. All animal experiments were conducted in compliance with the Guidelines for the Care and Use of Research Animals under protocols approved by the Animal Studies Committee of Washington University School of Medicine in St. Louis. The study was not pre-registered. MRI, PET scans and data acquisition are detailed in the method section. The arterial blood samples of subject A – C were collected for radioactive metabolite analysis during PET scans. Subjects D – G underwent baseline scans without collecting blood samples (Table 1). For the test-retest reproducibility studies within the same subject and among different subjects, subjects A–C underwent at least two PET imaging scans under baseline condition. For the same animal, the interval between repeating scans was at least 2 weeks. In addition, a blocking study was done in subject A by i.v. administration of (-)-vesamicol (0.125 mg/kg) about 5 min prior to the injection of [^{18}F]VAT.

MRI scans

For MRI scans, animals were initially anesthetized with ketamine at a dose of 10 to 20 mg/kg via intramuscular (i.m.) injection and glycopyrrolate at a dose of 0.13–0.017 mg/kg via i.m. injection, and intubated with an endotracheal tube under anesthesia, maintained at a dose of 0.75–2.0% isoflurane in oxygen throughout the procedure. MR images were acquired for each animal on a 3.0-T Trio or Prisma scanner (Siemens), using an 8-channel knee coil. The animal was positioned supine in a custom-made animal holder and stabilized with padding around the head. Rectal temperature was maintained within normal physiological range (37–38 °C) using a custom-built warm-air blanket. End-tidal O_2 saturation, body temperature, heart rate, and respiration rate were maintained within normal physiologic ranges and continuously monitored using MRI compatible physiological monitoring equipment (Precess, InVivo, Orlando, FL). Each NHP subject had the baseline MRI scan with a magnetization-prepared rapid acquisition gradient echo (MP-RAGE) sequence: repetition time = 2,400 ms, echo time = 3.93 ms, inversion time = 1,100 ms, FOV = 154 mm, flip angle = 8°, 208 sagittal slices, voxel size = 0.8 mm × 0.8 mm × 0.8 mm. The MR image volume was then cropped to 176 ×176 × 176 pixels and re-oriented into coronal

slices using the Analyze 12.0 software (AnalyzeDirect Inc., Overland Park, KS) for co-registration with PET images.

MicroPET imaging scans and data process

A microPET Focus 220 scanner (Concorde/CTI/Siemens Microsystems, Knoxville, TN) was used for the acquisition of imaging data for [^{18}F]VAT. For PET scans, animals were fasted for 12 h before each scan, initially anesthetized with ketamine at a dose of 10 to 20 mg/kg i.m. and glycopyrrolate at dose of 0.13 mg/kg i.m. and fitted with an endotracheal tube under anesthesia, maintained at 0.75–2.0% isoflurane in oxygen throughout the procedure. After intubation, a percutaneous venous catheter was placed for radiotracer injection. A 20-gauge plastic catheter was inserted into a femoral artery to permit arterial blood sampling. Blood pressure and pulse were monitored throughout the scan. Vital signs were monitored every 15 min, and core temperature was kept constant at 37 °C with heated water blankets. The head of the animal was positioned with the aid of a laser fixed within the PET scanning aperture. The head was firmly positioned with padding inside a modified head holder. In each microPET scan session, the head was positioned supine in the adjustable head holder with the brain in the center of the field of view. Attenuation characteristics of the head were determined individually prior to each study by obtaining a transmission scan. After that, the animal was administrated 378 ± 33 MBq (mean ± SD) of [^{18}F]VAT via the venous catheter. Subsequently, a 120-minute dynamic emission scan (3 × 1-min, 4 × 2-min, 3 × 3-min, and 20 × 5-min frames) was acquired.

The resolution of the reconstructed PET image was < 2.0 mm full width at half maximum for all 3 dimensions at the center of the field of view (Tai *et al.* 2005). Emission scans were corrected using individual attenuation and model-based scatter correction and reconstructed using filtered back projection as described previously(Miller *et al.* 1989). The first baseline PET image for each animal acted as the target image with the MRI (MPRAGE) and subsequent PETs co-registered to it using an automated image registration program AIR (Tabbal *et al.* 2006, Woods *et al.* 1993). For quantitative analyses, two-dimensional regions of interest (ROI) (cerebellar hemispheres, vermis, frontal cortex, occipital cortex, temporal cortex, striatum including caudate and putamen, white matter, midbrain and hippocampus) were drawn based on multiple lays of MRI brain images following the standard protocol, and transformed to the volume of interest (VOI) in Analyze 12.0 software (AnalyzeDirect Inc., Overland Park, KS) (Jin et al. 2016, Tu et al. 2015). The VOIs were transformed to the baseline PET space and then overlaid on all reconstructed PET images to obtain tissue time–activity curves in a homemade program Vidi (Jin et al. 2016, Tu et al. 2015). Radioactivity measures were standardized to body weight and dose of radioactivity injected to yield normalized brain radioactivity (kBq/mL) or standardized uptake value (SUV).

Whole blood and plasma collection for arterial blood input function

To determine the radioactive metabolite for correction of the arterial input function, arterial blood samples were collected from the femoral artery at different time points after the injection of [^{18}F]VAT. Continuous and sequential discrete arterial blood samples were collected during the first 2 min using an automatic blood drawer with a peristaltic pump that pulls arterial blood through a radioactivity detector composed of a plastic scintillator as we

previously published(Jin et al. 2016). Additional arterial samples (2 – 3 mL) were collected in heparinized syringes manually at 2, 5, 10, 15, 30, 60, 90 and 120 min after tracer injection for measurements of radiolabeled metabolites. HPLC radioactive metabolite analysis followed our published protocol (Jin et al. 2016). The percentiles of the plasma in whole blood (~60–70%) determined from the samples collected manually (2–120 min) were used to correct the plasma radioactivity curve for automatic sampling (0–2 min). The percentile of unmetabolized [^{18}F]VAT in the manually collected samples were determined from HPLC radioactive metabolite analysis. A metabolite-corrected plasma curve was used as input function [Cp(t)] for the kinetics and graphics analysis in a Matlab program (MathWorks Inc., Natick, MA).

Radio-metabolite analysis using HPLC

Radioactivity in whole blood (1 mL) was counted in a well gamma counter (Beckman Instruments Inc., NY), then centrifuged at 2,500 g in an Eppendorf 5415C centrifuge (Eppendorf North America, Inc.) for 5 min to separate red blood cells from plasma. Portions of plasma (400 μL) were solvent-deproteinated using 0.92 mL ice-cold methanol and separated by centrifugation for 3 min at 2,500 g. The supernatant of the centrifuged blood sample was mixed with water (1/1, v/v) and 180 μL of mixture was injected into a HPLC system for determination of radioactive metabolites. The HPLC system consisted of an Agilent SB C-18 analytic HPLC column (250 mm × 4.6 mm, 5 μm) and a UV detector with wavelength set at 254 nm. The mobile phase was composed of acetonitrile/ 0.1 M ammonium formate buffer (48/52, v/v, pH 4.5), and the flow rate was 1.0 mL/min. The HPLC fractions were collected at 1 min intervals for 16 min; each fraction was counted using a well gamma counter to determine the radioactivity. The results were corrected for background radiation and physical decay. The sample recovery yield, extraction efficiency, and HPLC fraction recovery were calculated by measuring radioactivity in the plasma HPLC fractions. The plasmid parent fraction was determined as the ratio of the radioactivity of the parent (standard) compound to the total plasmid amount of radioactivity collected.

Modeling methods

To quantitatively assess the radiotracer transfer between plasma, brain, and VAChT, seven different model-based kinetics methods were performed in this study(Ichise & Ballinger 1996, Logan *et al.* 1994, Logan *et al.* 1990, Lammertsma *et al.* 1996, Lammertsma & Hume 1996). Four of these seven methods need arterial blood sampling for blood input correction and they were the one-tissue compartment model (1TCM), two-tissue compartment model (2TCM), Logan graphic analysis (LoganAIF) and multiple linear analysis (MA1). The remaining three methods were based on reference modeling and they were the reference tissue model (RTM), simplified reference tissue model (SRTM), and Logan graphic analysis (LoganREF). Total volume distribution (VT), distribution volume ratio (DVR), the nondisplaceable binding potential (BP_{ND}) and other parameters were calculated accordingly. To establish the time dependence of BP_{ND} estimates, The BP_{ND} in the striatum was calculated by SRTM and LoganREF using entire 120-min recordings, and with truncation to 90, 60, 45 mins, and always with exclusion of the first 20 mins from the Logan linearization.

In the regression, the fits were performed with optimization of Chi-square (χ^2), which was the sum of the squared discrepancies between data and model predictions divided by the number of degrees of freedom. The cycle of χ^2 calculation and parameter adjustment was repeated until further reduction of χ^2 was not possible. The final set of parameters was regarded as the best-fit result. The independence of parameters was also assessed by a standard error (SE) via examining the covariance of the parameter (Gavin 2016). All non-linear regression modeling was solved by nonlinear least square fitting (NLSF) using the Marquart-Levenberg algorithm implemented in the Matlab function lm.m(Gavin 2016) (MathWorks Inc., Natick, MA). Relative standard error (rSE), which equals the SE value divided by the mean value, was also calculated to reveal the reliability of the estimation of each parameter.

In addition, the Lassen plot (Cunningham *et al.* 2010) was used to estimate non-displaceable distribution volume (V_{ND}) of [^{18}F]VAT in brain using the difference in VT at baseline and after partial blockade with (-)-vesamicol (0.125 mg/kg).

Model comparison and correlation analysis

Goodness of fit for 7 modeling methods were compared using model selection criterion (MSC)(Fujita *et al.* 1999) which was a simplified version applied to PET data analysis based on the original concept of AIC (Akaike information criterion) (Akaike 1974). The preferred model is the one with the highest MSC value. The value of χ^2 also provided a useful measure of goodness-of-fit. If the model described the measured data, the value of χ^2 would mostly represent the variance of the data and were close to 0. Regarding the correlation of these modeling methods, Pearson correlation was performed according to the procedure in the statistics section below.

Test-retest reproducibility studies

The BP_{ND} values from the model fitting of the SRTM and LoganREF were applied for the test-retest reproducibility. The test-retest study was performed with three NHP subjects A, B, and C (Table 1) to evaluate the variability of the relevant outcome for BP_{ND}. Each subject was studied twice, for which the physiology of the NHP and experimental conditions were identical. The test-retest variability (TRV) was then calculated for each region as follows:

$$TRV\,\% = 100 \times \frac{1}{n} \times \sum_{i=1}^{n} \frac{\left|BP_{ND}^{-i-test} - BP_{ND}^{-i+retest}\right|}{\frac{(BP_{ND}^{-i-test} - BP_{ND}^{-i-retest})}{2}} \quad (2)$$

Intraclass correlation coefficient also was calculated as follows:

$$ICC = \frac{MSBSS - MSWSS}{BSMSS + WSMSS} \quad (3)$$

Where MSBSS and MSWSS were the mean sum of squares between and within subjects, respectively; n was the number of within-subject measurements, in this study, n = 3. ICC

was the ratio of between-subject variances to total variance and the appropriate metric for assessing within-subject reliability. Therefore, ICC values was particularly high if within-subject (i.e. within-subject between sessions) variance was high.

Statistics

For modeling method comparison, the F-test (Hawkins *et al.* 1986) provided a comparison of the goodness-of-fit in striatum across all models. A p value of greater than 0.05 indicates that the PET data and the modeling data are not significantly different. Regarding the correlation of these modeling methods, Pearson correlation between BP_{ND} calculated with different brain regions using various models were analyzed to calculate Pearson's coefficients (r), and the p-value was obtained using Prism software (GraphPad Software, Inc). In addition, t test was used to determine the difference in test and retest values. A p value of less than 0.05 indicates statistically significant difference.

Results

TAC of unmetabolized parental [^{18}F]VAT from NHP plasma samples

HPLC analysis of plasma samples from baseline scans of 3 NHP subjects revealed that over 60% of the total radioactivity was the parent [^{18}F]VAT in plasma and ~40% of the total radioactivity in plasma was attributed to polar metabolites after 20 min p.i. of the radiotracer. Based on our previous analysis, the radioactive metabolites were significantly more polar than the parent compound (Tu et al. 2015). Therefore, radioactive metabolites do not likely penetrate the blood-brain barrier and enter into the brain (Tu et al. 2015). The percentile of unmetabolized parental [^{18}F]VAT in plasma decreased throughout the time course, from 96% ± 1% at 2 min, to 14% ± 2.7% at 90 min post-injection, respectively, as shown in Figure 1C. Although the actually structure was not confirmed by LC-MS, the rebuilding HPLC fraction collection radiochromatogram indicate the retention time of the major radioactive metabolite was 2–4 min compared to the retention time of 9–11 min for the parent compound [^{18}V]VAT, suggesting the major metabolite don't have the capability in crossing the blood brain barrier and entering into the brain(Tu *et al.* 2015). The average TAC curves were obtained from three subjects for the parental compound [^{18}F]VAT in plasma and in the brain regions (Figure 1B). The top part of Figure 1B showed that the concentration of parental compound [^{18}F]VAT in plasma peaked less than 1 min post-injection, and then rapidly washed out, but the specific binding to the brain regions peaked and then maintained.

Tracer kinetics analysis with different modeling

Radiotracer [^{18}F]VAT readily entered the brain and heterogeneously distributed. PET imaging data from the summed images of the dynamic scan from 0 to 120 min in animals at baseline condition are depicted in Figure 1. The striatum has the highest accumulation of [^{18}F]VAT, followed by thalamus, hippocampus, frontal cortex and cerebellum. Characterization of the tracer kinetics (in striatum and other brain regions) with different modeling methods including 2TCM, 1TCM, MA1 (Figure 2) and LoganAIF with arterial blood input function, and RTM, SRTM, and LoganREF with the reference region as input function were performed for 0–120 min dynamic scans of [^{18}F]VAT in three subjects. The modeling results are summarized in Table 2. The BP_{ND} values were consistent across all

these modeling methods with small standard deviation (SD), while the V_T values showed larger intra-subject variations and SD values shown in Table 2, suggesting BP_{ND} was more consistent than V_T in these estimations.

For the modeling of striatal kinetics with arterial blood input function, including 2TCM, 1TCM, LoganAIF and MA1, based on the MSC, χ^2 and F-test p-values, the 2TCM and LoganAIF models proved more appropriate than the 1TCM or MA1 models (Table 2 and Figure 2). The baseline kinetics of striatum was also estimated using the reference-based models in total 7 NHPs, as shown in Table 2 and Table 4. For the reference based modeling methods, RTM, SRTM, and LoganREF models, all provided appropriate fittings. Overall, the 2TCM model is most appropriate among the methods with arterial blood input function, and the SRTM model is most appropriate among the methods based on reference without blood input, as shown in Table 2.

Using the 2TCM method, the tracer kinetics for different brain regions were characterized and summarized in Table 3. The 2TCM method offered reasonable calculations of K_1, k_2, k_3 and k_4 values, but the small values of k_3 and k_4, led to large SDs of these parameter estimates. As a consequence, values of V_T were highly variable between subjects. The rank of V_T values (mL/cm^{-3}) from high to low were: striatum, thalamus, hippocampus, frontal cortex, vermis, occipital cortex, temporal cortex, white matter, midbrain and cerebellum-hemispheres. Although the V_T showed large SD, the BP estimated from k_3/k_4 ratios was less variable between subjects. Values of k_3/k_4 estimated are also summarized in Table 3. The rank of values from high to low is: striatum, thalamus, hippocampus, frontal cortex, vermis, occipital cortex, temporal cortex, white matter, midbrain and cerebellum-hemispheres. Compared to V_T or k_3/k_4, the BP_{ND} (DVR-1) values were estimated with the smallest SD. And the rank order of BP_{ND} values are consistent with the rank order of VAChT density in brain regions. At baseline conditions, the highest BP_{ND} (DVR-1) value (mean ± SD) was observed in the striatum (3.37 ± 0.34), intermediate levels were observed in thalamus (1.16 ± 0.24), hippocampus (0.61 ± 0.41), frontal cortex (0.44 ± 0.10) and vermis (0.22 ± 0.55) regions, and lowest BP_{ND} values were observed in the white matter (0.21± 0.13) and cerebellum-hemispheres. This is consistent with literature reports that these regions have relatively lower expression of VAChT (Efange et al. 2000, Efange 2000, Weihe *et al.* 1996).

To estimate the V_{ND} of [^{18}F]VAT and to further verify the suitability of cerebellar hemispheres as the reference region, the data from a blocking study using a VAChT specific inhibitor (-)-vesamicol (0.125mg/kg) and one baseline data from the same monkey (subject A) was analyzed. The result showed partial blockade was achieve by ~54% and the V_{ND} was ~1.27,which was slightly lower than the V_T value of cerebellar hemispheres (Figure 5). Due to the inaccuracy in quantification in low binding regions, the difference may be overestimated. As a result, cerebellar hemispheres is suitable as the reference region for [^{18}F]VAT kinetic modeling analysis using reference based methods.

Using the reference based method, different brain regions other than cerebellum-hemispheres were characterized and summarized in Table 4. Both SRTM and LoganREF provided heterogeneous binding profiles for the different brain regions, as did 2TCM. The rank of the specific binding from LoganREF (Figure 3) was: striatum > thalamus >

hippocampus > frontal cortex, based on the BP_{ND} values estimated (mean ± SD): 2.11 ± 0.43, 0.76 ± 0.3, 0.47 ± 0.3 and 0.29 ± 0.2 respectively, with cerebellum-hemispheres as the reference. The rank of the specific binding calculated from SRTM was identical to that calculated from LoganREF: striatum > thalamus > hippocampus > frontal cortex, with the BP_{ND} values of 2.15 ± 0.46, 0.79 ± 0.3, 0.48 ± 0.2 and 0.32 ± 0.2 respectively. These rank of specific binding were consistent to the 2TCM method. In addition, the striatal BP_{ND} values were estimated by SRTM and LoganREF using entire 120-min recordings and with truncation to 90, 60, 45 mins, to establish the time dependence of BP_{ND} estimates (Table 5). The data indicated BP_{ND}-SRTM values had no significant change when the scan duration for analysis reduced from 120 min to 60 min. Meanwhile, BP_{ND}-LoganREF values were impacted by the truncation of scan duration.

Correlations between modeling methods

To investigate the correlation of all seven modeling methods (2TCM, 1TCM, MA1, LoganAIF, RTM, SRTM, and LoganREF), Pearson's correlation tests were carried out using BP_{ND} estimates of different brain regions from a total of 3 individual scans of 3 NHP subjects. The Pearson's coefficients (r) are summarized in Table 6A and the p-values are presented in Table 6B. Overall correlation data in Table 6 suggest that modeling methods with a reference had lower p-values and higher Pearson's coefficients (r). Regarding the correlation between modeling methods with arterial blood input and the methods based on reference, SRTM had the highest positive correlation to 2TCM (r = 0.958) with a p-value of 0.021 as displayed in Table 6 and Figure 4A, while RTM had less positive correlation to 2TCM (r = 0.940) with a p-value of 0.030 (Figure 4B). The LoganREF had the third highest positive correlation to 2TCM (r = 0.932) with a p-value of 0.034 as shown in Table 6 and Figure 4C. The SRTM BP_{ND} estimates indicated a strong correlation with those obtained from LoganREF with r = 0.994, p-value 0.003 as shown in Table 6 and Figure 4D. Moreover, the BP_{ND} estimates using LoganAIF were also in good agreement with those from LoganREF (r = 0.943, p-value 0.029), and LoganREF (r = 0.946, p = 0.027) with the cerebellum-hemispheres as reference region as shown in Table 6. From these correlation results, we found that reference-based modeling including both SRTM and LoganREF were able to provide kinetics parameters similar to modeling with arterial blood input functions. However, when choosing the proper modeling method, it should be taken into consideration that BP_{ND} values analyzed by reference-based modeling are always underestimated compared to 2TCM (2.1 vs 3.4). This might partly attributed to the inaccuracy in quantification in the low binding reference region cerebellar hemispheres.

Test-retest reproducibility

The reliability of the PET measurement was demonstrated by a relatively low variability in repeated measurements of BP_{ND} in the high-binding brain regions, including striatum, thalamus, frontal cortex and hippocampus, as shown in Table 7. Global mean values of TRV % were less than 9%. Both TRVs using SRTM and LogaREF were comparable. For each outcome parameter, the mean of the test and retest scans, the TRV% (mean ± SD), and the ICC from either LoganREF or SRTM are summarized in Tables 7A and 7B. The TRV% of BP_{ND} values in different brain regions from LoganREF were striatum 7.91 ± 0.67; thalamus 4.99 ± 0.09; hippocampus 0.95 ± 0.17; and frontal cortex 4.65 ± 0.06, while TRV% from

BP-SRTM are striatum 8.38 ± 0.62; thalamus 0.36 ± 0.11; hippocampus 4.47 ± 0.13; and frontal cortex 8.64 ± 0.05. All TRV values are smaller than 10%, indicating that no systematic trend existed between test and retest scans. The ICC values from both LoganREF and SRTM are all greater than 0.72, indicating that BP_{ND} from all these regions is highly reproducible with small interclass errors.

Discussion

The goal of this study was to validate different modeling methods to quantitatively estimate the level of VAChT by analyzing the [^{18}F]VAT brain uptake data generated from PET scans in NHP subjects. Under baseline conditions, the regional distribution of [^{18}F]VAT uptake was concordant with the expression levels of VAChT in different regions of the brain (Jin et al. 2016, Petrou et al. 2014, Cyr et al. 2014). With limited statistical quality for the dynamic acquisitions of time-activity data, relatively simple models with 2 to 4 parameters such as 2TCM and 1TCM can be estimated. Kinetic analyses of [^{18}F]VAT brain uptake suggested that a 2TCM configuration provided much better fits than a 1TCM configuration. This was based on the comparison criteria including MSC, χ^2, and F-statistics. Despite a statistical superiority of the 2TCM model in describing [^{18}F]VAT time–activity data, the difference in V_T values obtained between a 1TCM and a 2TCM was small, especially at baseline conditions shown in Table 2.

2TCM modeling provided good assessment of K_1 under both baseline conditions from three NHP subjects. At steady-state they are independent of tracer delivery and give an index of transport site density (Logan et al. 1994). This view was supported by the observation that the rank order of V_T values correlated well with the order of VAChT densities reported in both the rat and human brain post mortem (Jin et al. 2016, Petrou et al. 2014, Cyr et al. 2014) and the *in vivo* human studies using [^{18}F]FEOBV tracer (Petrou et al. 2014).

All three NHP subjects with arterial blood input function examined using 2TCM-based methods gave similar estimates for V_T and BP_{ND}, and both parameters were estimated with high reproducibility. In addition, V_T values estimated using the three methods including 2TCM, 1TCM, MA1, were highly correlated, but estimation with the LoganAIF led to a slightly low V_T value. Incontrovertibly, the BP_{ND} values from all these models were correlated even with the methods from the references-based methods including RTM, SRTM, and LoganREF. Therefore, BP_{ND} appeared to be a valuable parameter for assessing the level of VAChT because of the high level of precision that were not impacted by subject differences in blood flow or peripheral clearance.

Previous VAChT PET tracers including [^{123}I]IBVM and [^{18}F]FEOBV required long scan times due to slow kinetics (Petrou et al. 2014, Kilbourn et al. 2009). Striatal uptake of [^{18}F]VAT peaked about 20 min after tracer injection and then gradually decreased. Here, quantitative kinetics analysis has demonstrated the *in vivo* binding potency and specificity of [^{18}F]VAT toward VAChT in nonhuman primates. Out of the different modeling methods, the 2TCM model was the more robust kinetics model. The Pearson's correlation tests indicate that modeling with reference showed very high correlation with 2TCM. Correlation analyses suggests the reference-based modeling including SRTM and LoganREF provided reliable

kinetics parameters. Therefore the reference-based modeling may be applied for kinetic quantification of [^{18}F]VAT without collecting arterial blood input functions.

In summary, the newly developed PET tracer [^{18}F]VAT demonstrated high in vivo binding potency for VAChT, and was a superb radioligand for quantifying cholinergic presynaptic terminals. This tracer has high specific *in vivo* uptake in the VAChT-enriched striatum whereas the cerebellum-hemisphere region has the lowest density of binding sites. The kinetics analyses indicated that a 2TCM model best describes [^{18}F]VAT kinetics; estimations of BP using reference methods without arterial blood samples were strongly correlated to 2TCM methods. The reproducibility study demonstrated a low variability in repeated measurements of BP_{ND} in the high binding brain regions including striatum, thalamus, frontal cortex and hippocampus. The results of the present study support the suitability of using [^{18}F]VAT for the quantitative measure of VAChT densities in humans using PET.

Conclusion

Radiotracer [^{18}F]VAT is a promising PET radiotracer for quantitative visualization of VAChT *in vivo*. The high retention order of [^{18}F]VAT is in the striatum, thalamus, hippocampus, frontal cortex, and vermis. Kinetics modeling indicated that the 2TCM modeling method provides markedly better fits to the data than 1TCM or MA1 fits with arterial blood sampling. The SRTM or LoganREF fit can provide a consistent BP_{ND} value similar to the 2TCM fit with cerebellum-hemispheres as the reference region. These results demonstrate that [^{18}F]VAT is a suitable PET radioligand for imaging VAChT *in vivo.* This promising radiotracer warrants further clinical investigation in human subjects.

Acknowledgments

The authors thank the Cyclotron Facility of Washington University School of Medicine. Authors also thank Emily William, Christina Zukas, Darryl Craig, and John Hood for technique support. This work was supported by USA National Institute of health (NIH)/National Institute of Neurological Disorders and Stroke (NINDS), National Institute on Aging (NIA), and National Institute of Mental Health (NIMH) NS075527, NS103988, NS061025, NS058714, MH092797), and the U.S.A. Department of Energy (DES0012737); the Barnes Jewish Hospital Foundation (Elliot Stein Fund and Parkinson Disease Research Fund).

Abbreviations

ACh	acetylcholine
AChE	acetylcholinesterase
AD	Alzheimer’s disease
AIR	automated image registration
BP_{ND}	binding potential (non-displaceable)
CNS	central nervous system
EOB	end of bombardment
DVR	distribution volume ratio

[^{18}F]-FEOBV	(–)-5-^{18}F-fluoroethoxybenzovesamicol
[^{18}F]VAT	((-)-(1-(-8-(2-fluoroethoxy)-3-hydroxy-1,2,3,4-tetrahydronaphthalen-2-yl)piperidin-4-yl)(4-fluorophenyl)-methanone)
h	hour
HD	Huntington's disease
HPLC	high-performance liquid chromatography
i.v.	intravenous injection
i.m.	intramuscular
K_1	transfer constant from plasma (C_p) to specific target tissue (C_1) (mL g^{-1} min^{-1})
k_2	transfer rate constant from tissue to plasma (min^{-1})
k_3	pseudo-first order associate rate constant for ligand-binding site (min^{-1})
k_4	first order dissociation rate constant for ligand-binding site (min^{-1}).
K_d	equilibrium dissociation constant
LoganAIF	Logan graphic modeling with arterial input function
LoganREF	Logan graphic modeling with reference
MA1	multiple linear modeling with arterial blood input function
MSC	model selection criterion
MP-RAGE	magnetization-prepared rapid gradient echo
NHPs	nonhuman primates
NLSF	nonlinear least square fitting
PD	Parkinson's disease
PET	positron emission tomography
p.i.	post injection
ROI	region of interest
RTM	reference tissue model
SPECT	single-photon emission computed tomography
SRTM	simplified reference tissue model

SD	standard deviation
SE	standard error
SUV	standardized uptake value
TAC	time activity curve
1TCM	one-tissue compartment model
2TCM	two-tissue compartment model
VAChT	vesicular acetylcholine transporter
V_T	total volume of distribution.

References

Aghourian M, Legault-Denis C, Soucy JP, Rosa-Neto P, Gauthier S, Kostikov A, Gravel P, Bedard MA. Quantification of brain cholinergic denervation in Alzheimer's disease using PET imaging with [(18)F]-FEOBV. Mol Psychiatry. 2017; 22:1531–1538. [PubMed: 28894304]

Akaike H. New Look at Statistical-Model Identification. Ieee T Automat Contr. 1974; Ac19:716–723.

Anderson DC, Bahr BA, Parsons SM. Stoichiometries of acetylcholine uptake, release, and drug inhibition in Torpedo synaptic vesicles: heterogeneity in acetylcholine transport and storage. Journal of neurochemistry. 1986; 46:1207–1213. [PubMed: 3950624]

Barret O, Mazere J, Seibyl J, Allard M. Comparison of noninvasive quantification methods of in vivo vesicular acetylcholine transporter using [123I]-IBVM SPECT imaging. Journal of cerebral blood flow and metabolism : official journal of the International Society of Cerebral Blood Flow and Metabolism. 2008; 28:1624–1634.

Bohnen NI, Albin RL. The cholinergic system and Parkinson disease. Behavioural brain research. 2011; 221:564–573. [PubMed: 20060022]

Bohnen NI, Kaufer DI, Ivanco LS, Lopresti B, Koeppe RA, Davis JG, Mathis CA, Moore RY, DeKosky ST. Cortical cholinergic function is more severely affected in parkinsonian dementia than in Alzheimer disease: an in vivo positron emission tomographic study. Archives of neurology. 2003; 60:1745–1748. [PubMed: 14676050]

Bohnen NI, Muller ML, Kuwabara H, Constantine GM, Studenski SA. Age-associated leukoaraiosis and cortical cholinergic deafferentation. Neurology. 2009; 72:1411–1416. [PubMed: 19380700]

Braak H, Ghebremedhin E, Rub U, Bratzke H, Del Tredici K. Stages in the development of Parkinson's disease-related pathology. Cell and tissue research. 2004; 318:121–134. [PubMed: 15338272]

Cunningham VJ, Rabiner EA, Slifstein M, Laruelle M, Gunn RN. Measuring drug occupancy in the absence of a reference region: the Lassen plot re-visited. Journal of cerebral blood flow and metabolism : official journal of the International Society of Cerebral Blood Flow and Metabolism. 2010; 30:46–50.

Cyr M, Parent MJ, Mechawar N, et al. PET imaging with [(1)(8)F]fluoroethoxybenzovesamicol ([(1)(8)F]FEOBV) following selective lesion of cholinergic pedunculopontine tegmental neurons in rat. Nuclear medicine and biology. 2014; 41:96–101. [PubMed: 24267056]

Cyr M, Parent MJ, Mechawar N, Rosa-Neto P, Soucy JP, Clark SD, Aghourian M, Bedard MA. Deficit in sustained attention following selective cholinergic lesion of the pedunculopontine tegmental nucleus in rat, as measured with both post-mortem immunocytochemistry and in vivo PET imaging with [(1)(8)F]fluoroethoxybenzovesamicol. Behavioural brain research. 2015; 278:107–114. [PubMed: 25257103]

Efange SM. In vivo imaging of the vesicular acetylcholine transporter and the vesicular monoamine transporter. FASEB journal : official publication of the Federation of American Societies for Experimental Biology. 2000; 14:2401–2413. [PubMed: 11099458]

Efange SM, Khare AB, von Hohenberg K, Mach RH, Parsons SM, Tu Z. Synthesis and in vitro biological evaluation of carbonyl group-containing inhibitors of vesicular acetylcholine transporter. Journal of medicinal chemistry. 2010; 53:2825–2835. [PubMed: 20218624]

Efange SM, von Hohenberg K, Khare AB, Tu Z, Mach RH, Parsons SM. Synthesis and biological characterization of stable and radioiodinated (±)-trans-2-hydroxy-3-P[4-(3-iodophenyl)piperidyl]-1,2,3,4-tetrahydronaphthalen e (3′-IBVM). Nuclear medicine and biology. 2000; 27:749–755. [PubMed: 11150707]

Fujita M, Seibyl JP, Verhoeff NP, et al. Kinetic and equilibrium analyses of [(123)I]epidepride binding to striatal and extrastriatal dopamine D(2) receptors. Synapse (New York, N Y). 1999; 34:290–304.

Gavin, HP. Structural Dynamics and the Seismic Response Control Laboratory. Department of Civil and Environmental Engineering, Duke University; 2016. The Levenberg-Marquardt method for nonlinear least squares curve-fitting problems.

Giboureau N, Emond P, Fulton RR, et al. Ex vivo and in vivo evaluation of (2R,3R)-5-[(18)F]-fluoroethoxy- and fluoropropoxy-benzovesamicol, as PET radioligands for the vesicular acetylcholine transporter. Synapse. 2007; 61:962–970. [PubMed: 17787004]

Haense C, Kalbe E, Herholz K, Hohmann C, Neumaier B, Krais R, Heiss WD. Cholinergic system function and cognition in mild cognitive impairment. Neurobiology of aging. 2012; 33:867–877. [PubMed: 20961662]

Hawkins RA, Phelps ME, Huang SC. Effects of temporal sampling, glucose metabolic rates, and disruptions of the blood-brain barrier on the FDG model with and without a vascular compartment: studies in human brain tumors with PET. Journal of cerebral blood flow and metabolism : official journal of the International Society of Cerebral Blood Flow and Metabolism. 1986; 6:170–183.

Ichise M, Ballinger JR. From graphical analysis to multilinear regression analysis of reversible radioligand binding. Journal of cerebral blood flow and metabolism : official journal of the International Society of Cerebral Blood Flow and Metabolism. 1996; 16:750–752.

Jin H, Zhang X, Yue X, et al. Kinetics modeling and occupancy studies of a novel C-11 PET tracer for VAChT in nonhuman primates. Nuclear medicine and biology. 2016; 43:131–139. [PubMed: 26872437]

Karimi M, Tu Z, Yue X, Zhang X, Jin H, Perlmutter JS, Laforest R. Radiation dosimetry of [(18)F]VAT in nonhuman primates. EJNMMI research. 2015; 5:73. [PubMed: 26660544]

Kawamura K, Shiba K, Tsukada H, Nishiyama S, Mori H, Ishiwata K. Synthesis and evaluation of vesamicol analog (-)-O-[11C]methylvesamicol as a PET ligand for vesicular acetylcholine transporter. Annals of nuclear medicine. 2006; 20:417–424. [PubMed: 16922470]

Kilbourn MR, Hockley B, Lee L, Sherman P, Quesada C, Frey KA, Koeppe RA. Positron emission tomography imaging of (2R,3R)-5-[^{18}F]fluoroethoxybenzovesamicol in rat and monkey brain: a radioligand for the vesicular acetylcholine transporter. Nuclear medicine and biology. 2009; 36:489–493. [PubMed: 19520289]

Lammertsma AA, Bench CJ, Hume SP, Osman S, Gunn K, Brooks DJ, Frackowiak RS. Comparison of methods for analysis of clinical [11C]raclopride studies. Journal of cerebral blood flow and metabolism : official journal of the International Society of Cerebral Blood Flow and Metabolism. 1996; 16:42–52.

Lammertsma AA, Hume SP. Simplified reference tissue model for PET receptor studies. NeuroImage. 1996; 4:153–158. [PubMed: 9345505]

Li J, Zhang X, Zhang Z, et al. Heteroaromatic and aniline derivatives of piperidines as potent ligands for vesicular acetylcholine transporter. Journal of medicinal chemistry. 2013; 56:6216–6233. [PubMed: 23802889]

Logan J, Fowler JS, Volkow ND, et al. Graphical analysis of reversible radioligand binding from time-activity measurements applied to [N-11C-methyl]-(-)-cocaine PET studies in human subjects. Journal of cerebral blood flow and metabolism : official journal of the International Society of Cerebral Blood Flow and Metabolism. 1990; 10:740–747.

Logan J, Volkow ND, Fowler JS, et al. Effects of blood flow on [11C]raclopride binding in the brain: model simulations and kinetic analysis of PET data. Journal of cerebral blood flow and

metabolism : official journal of the International Society of Cerebral Blood Flow and Metabolism. 1994; 14:995–1010.

Mazere J, Meissner WG, Sibon I, Lamare F, Tison F, Allard M, Mayo W. [(123)I]-IBVM SPECT imaging of cholinergic systems in multiple system atrophy: A specific alteration of the ponto-thalamic cholinergic pathways (Ch5-Ch6). NeuroImage. Clinical. 2013; 3:212–217. [PubMed: 24179865]

Miller TR, Wallis JW, Wilson AD. Interactive reconstruction in single-photon tomography. European journal of nuclear medicine. 1989; 15:189–193. [PubMed: 2787746]

Nishiyama S, Ohba H, Kobashi T, Nakamasu Y, Nakao H, Ogata T, Kitashoji T, Tsukada H. Development of novel PET probe [(11) C](R,R)HAPT and its stereoisomer [(11) C](S,S)HAPT for vesicular acetylcholine transporter imaging: A PET study in conscious monkey. Synapse. 2014; 68:283–292. [PubMed: 24687885]

Parent M, Bedard MA, Aliaga A, et al. PET imaging of cholinergic deficits in rats using [18F]fluoroethoxybenzovesamicol ([18F]FEOBV). NeuroImage. 2012; 62:555–561. [PubMed: 22555071]

Parent MJ, Cyr M, Aliaga A, Kostikov A, Schirrmacher E, Soucy JP, Mechawar N, Rosa-Neto P, Bedard MA. Concordance between in vivo and postmortem measurements of cholinergic denervation in rats using PET with [18F]FEOBV and choline acetyltransferase immunochemistry. EJNMMI research. 2013; 3:70. [PubMed: 24103360]

Petrou M, Frey KA, Kilbourn MR, Scott PJ, Raffel DM, Bohnen NI, Muller ML, Albin RL, Koeppe RA. In vivo imaging of human cholinergic nerve terminals with (-)-5-^{18}F-fluoroethoxybenzovesamicol: biodistribution, dosimetry, and tracer kinetic analyses. Journal of nuclear medicine : official publication, Society of Nuclear Medicine. 2014; 55:396–404.

Pirker W, Holler I, Gerschlager W, Asenbaum S, Zettinig G, Brucke T. Measuring the rate of progression of Parkinson's disease over a 5-year period with beta-CIT SPECT. Movement disorders : official journal of the Movement Disorder Society. 2003; 18:1266–1272. [PubMed: 14639666]

Prado VF, Roy A, Kolisnyk B, Gros R, Prado MA. Regulation of cholinergic activity by the vesicular acetylcholine transporter. The Biochemical journal. 2013; 450:265–274. [PubMed: 23410039]

Ransome MI, Hannan AJ. Behavioural state differentially engages septohippocampal cholinergic and GABAergic neurons in R6/1 Huntington's disease mice. Neurobiology of learning and memory. 2012; 97:261–270. [PubMed: 22261461]

Sharrad DF, de Vries E, Brookes SJ. Selective expression of alpha-synuclein-immunoreactivity in vesicular acetylcholine transporter-immunoreactive axons in the guinea pig rectum and human colon. The Journal of comparative neurology. 2013a; 521:657–676. [PubMed: 22821666]

Sharrad DF, Gai WP, Brookes SJ. Selective coexpression of synaptic proteins, alpha-synuclein, cysteine string protein-alpha, synaptophysin, synaptotagmin-1, and synaptobrevin-2 in vesicular acetylcholine transporter-immunoreactive axons in the guinea pig ileum. The Journal of comparative neurology. 2013b; 521:2523–2537. [PubMed: 23296877]

Shiba K, Ogawa K, Ishiwata K, Yajima K, Mori H. Synthesis and binding affinities of methylvesamicol analogs for the acetylcholine transporter and sigma receptor. Bioorganic & medicinal chemistry. 2006; 14:2620–2626. [PubMed: 16434200]

Tabbal SD, Mink JW, Antenor JA, Carl JL, Moerlein SM, Perlmutter JS. 1-Methyl-4-phenyl-1,2,3,6-tetrahydropyridine-induced acute transient dystonia in monkeys associated with low striatal dopamine. Neuroscience. 2006; 141:1281–1287. [PubMed: 16766129]

Tai YC, Ruangma A, Rowland D, Siegel S, Newport DF, Chow PL, Laforest R. Performance evaluation of the microPET focus: a third-generation microPET scanner dedicated to animal imaging. Journal of nuclear medicine : official publication, Society of Nuclear Medicine. 2005; 46:455–463.

Tu Z, Efange SM, Xu J, Li S, Jones LA, Parsons SM, Mach RH. Synthesis and in vitro and in vivo evaluation of ^{18}F-labeled positron emission tomography (PET) ligands for imaging the vesicular acetylcholine transporter. Journal of medicinal chemistry. 2009; 52:1358–1369. [PubMed: 19203271]

Tu Z, Wang W, Cui J, Zhang X, Lu X, Xu J, Parsons SM. Synthesis and evaluation of in vitro bioactivity for vesicular acetylcholine transporter inhibitors containing two carbonyl groups. Bioorganic & medicinal chemistry. 2012; 20:4422–4429. [PubMed: 22739089]

Tu Z, Zhang X, Jin H, et al. Synthesis and biological characterization of a promising F-18 PET tracer for vesicular acetylcholine transporter. Bioorganic & medicinal chemistry. 2015; 23:4699–4709. [PubMed: 26138195]

Wang W, Cui J, Lu X, Padakanti PK, Xu J, Parsons SM, Luedtke RR, Rath NP, Tu Z. Synthesis and in vitro biological evaluation of carbonyl group-containing analogues for sigma1 receptors. Journal of medicinal chemistry. 2011; 54:5362–5372. [PubMed: 21732626]

Weihe E, Tao-Cheng JH, Schafer MK, Erickson JD, Eiden LE. Visualization of the vesicular acetylcholine transporter in cholinergic nerve terminals and its targeting to a specific population of small synaptic vesicles. Proceedings of the National Academy of Sciences of the United States of America. 1996; 93:3547–3552. [PubMed: 8622973]

Woods RP, Mazziotta JC, Cherry SR. MRI-PET registration with automated algorithm. Journal of computer assisted tomography. 1993; 17:536–546. [PubMed: 8331222]

Yue X, Bognar C, Zhang X, Gaehle GG, Moerlein SM, Perlmutter JS, Tu Z. Automated production of [(1)(8)F]VAT suitable for clinical PET study of vesicular acetylcholine transporter. Applied radiation and isotopes : including data, instrumentation and methods for use in agriculture, industry and medicine. 2016; 107:40–46.

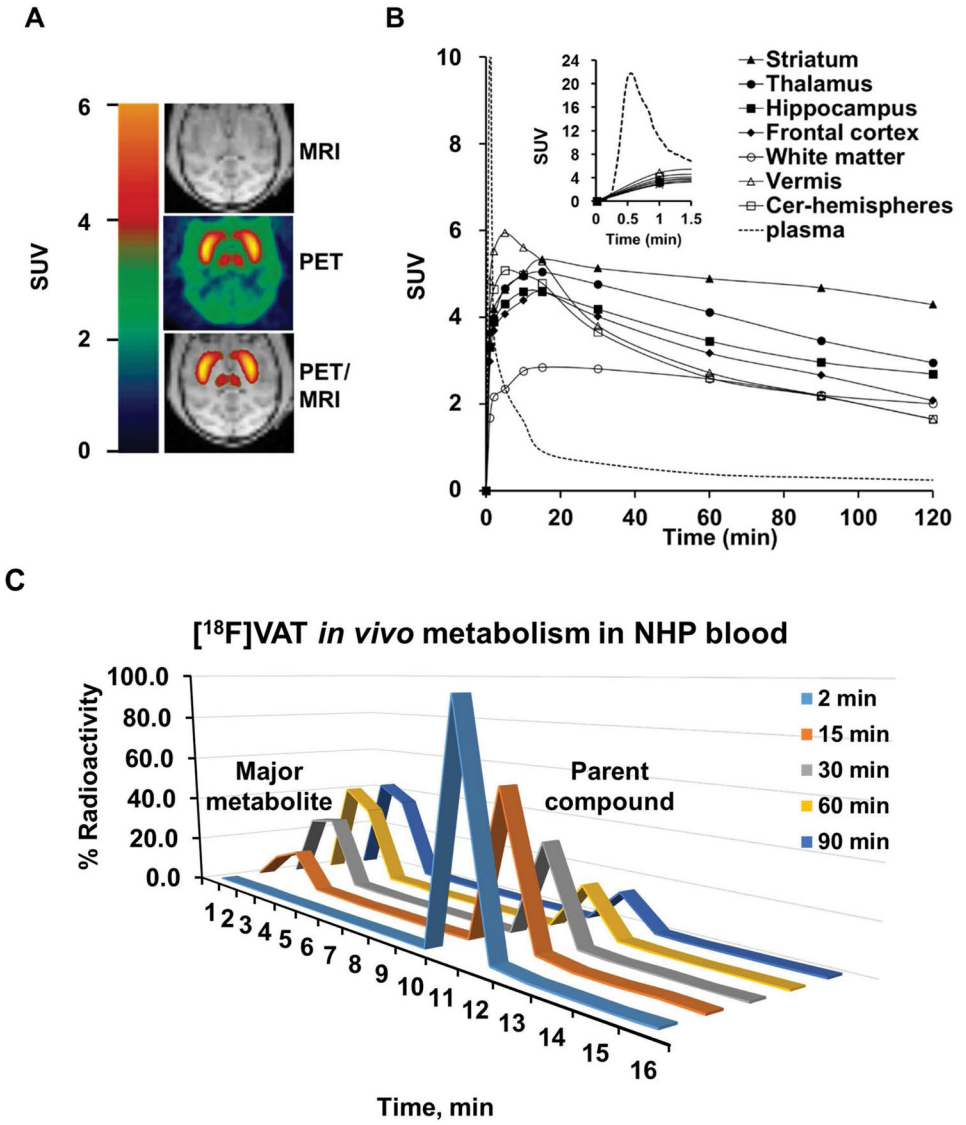

Figure 1. MicroPET studies of [^{18}F]VAT binding specificity in nonhuman primates

A. Representative brain imaging of [^{18}F]VAT collected from male cynomolgus macaques elucidate the high binding in striatum (caudate and putamen) and thalamus accumulations flanking the transverse axis, MRI (top), PET (middle), and PET/MRI-coregistered (bottom). **B.** Averaged time-activity curves of [^{18}F]VAT from three individual healthy male cynomolgus monkeys. Regional radioactivity (kBq/mL) curves for the unmetabolized [^{18}F]VAT in plasma (dashed line), and brain regions: striatum (filled triangles), thalamus(filled circles), hippocampus (filled squares), frontal cortex (filled diamonds), vermis (open triangles), white matter (open circles) and cerebellum-hemispheres (open squares). The insert figure is the zoom-in activity curve for the plasm in 1.5 min post injection. **C.** Representative radiochromatograms of [^{18}F]VAT from a plasma extract at different time points post tracer injection.

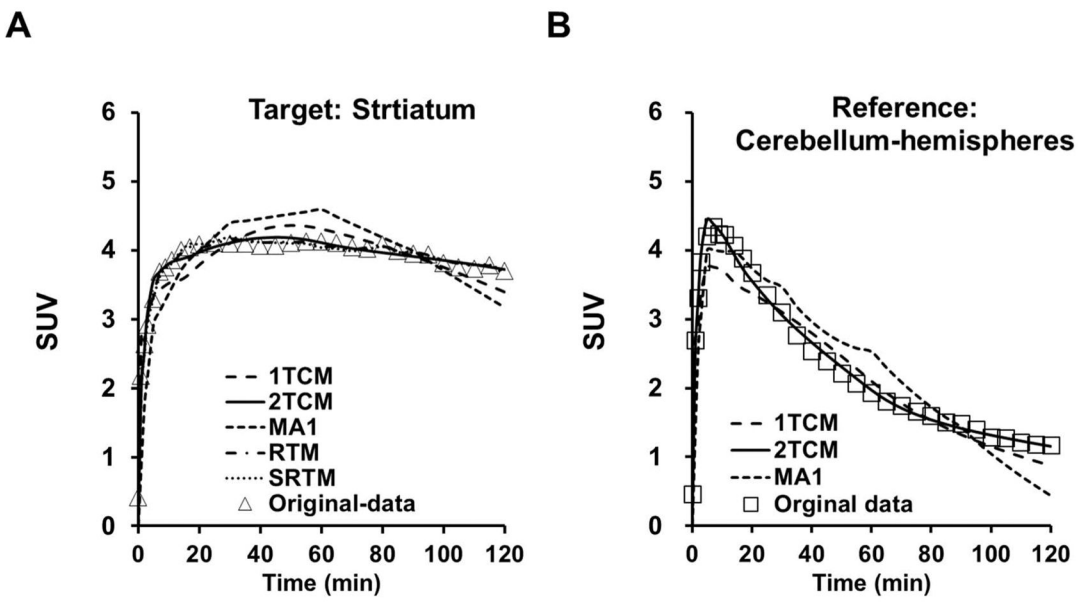

Figure 2. Kinetics model fitting with different non-linear modeling methods

A. Representative curve fitting for different modeling methods in the target region (striatum) time activity data: 1TCM (dashed line), 2TCM (solid line), MA1 (dashed line), RTM (broken dashed line), SRTM (dotted line) and original data (open triangles); **B**. Representative curve fitting for different modeling methods in the reference region (cerebellum-hemispheres) time activity data: 1TCM (dashed line), 2TCM (solid line), MA1 (dashed line), RTM (broken dashed line), SRTM (dotted line) and original data (open triangles).

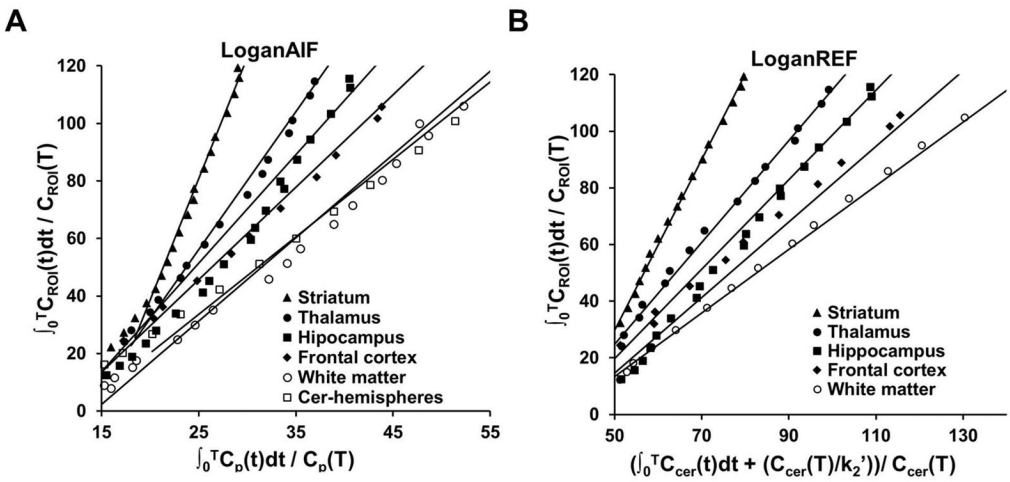

Figure 3. Kinetics model fitting with Logan graphic methods

A. Representative time activity curve fitting for LoganAIF with different brain regions: striatum (filled triangles), thalamus (filled circles), hippocampus (filled squares), white matter (open circles), and cerebellum-hemispheres (open squares). **B**. Representative time activity curve fitting for LoganREF with different brain regions: striatum (filled triangles), thalamus (filled circles), hippocampus (filled squares), and white matter (open circles) while cerebellum-hemispheres were the reference region.

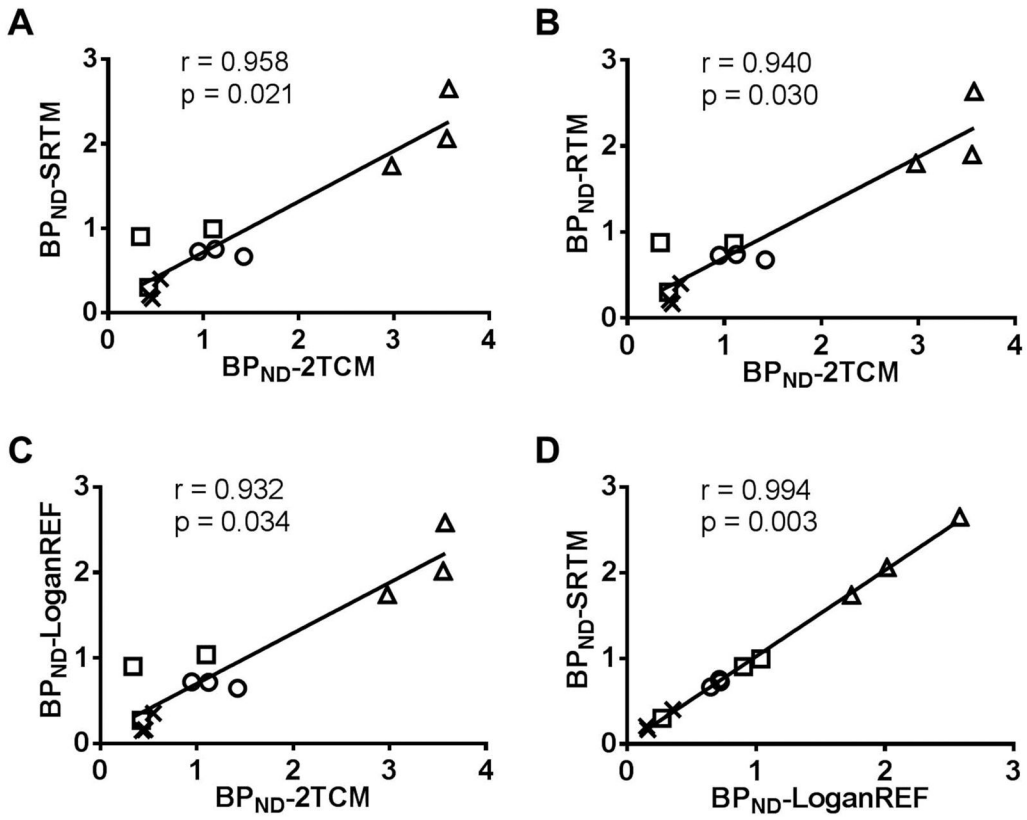

Figure 4. Scatter plot correlation between modeling methods

A. Scatter plot of all brain regions BP_{ND} from SRTM versus 2TCM suggested that SRTM has strong positive correlation to 2TCM (r = 0.958, p = 0.021). **B.** RTM versus 2TCM suggested that RTM has positive correlation to 2TCM (r = 0.940, p = 0.030), but less than SRTM versus 2TCM. **C.** LoganREF also has a strong positive correlation to the 2TCM modeling (r = 0.932, p = 0.034). **D**. There was a high positive correlation between SRTM and LoganREF (r = 0.994, p = 0.003). △: striatum; ○: thalamus; □: hippocampus; x: frontal cortex.

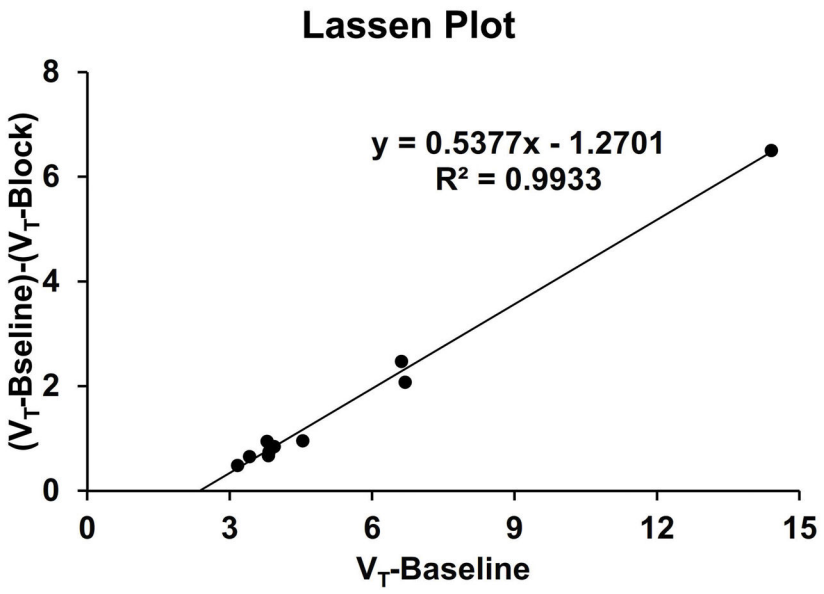

Figure 5. Lassen Plot to estimate nondisplaceable distribution volume (V_{ND}) of [^{18}F]VAT in brain

The data from a blocking study using a VAChT specific inhibitor (-)-vesamicol (0.125mg/kg) and one baseline data from the same monkey (subject A) was analyzed. The result showed partial blockade was achieve by ~54% and the V_{ND} was ~1.27,which was slightly lower than the V_T value of cerebellar hemispheres.

Table 1

Summary of NHP subjects in this study

NHP subject	Age (y)	Weight (kg)	Scans with arterial blood input	Scans without arterial blood input	Scans for test-retest	Blocking
A	**7**	**5.8**	√	√	√	√
B	**8**	**6.7**	√	√	√	
C	**6**	**9.1**	√	√	√	
D	**7**	**7.1**		√		
E	**6**	**8.8**		√		
F	**7**	**8.2**		√		
G	**7**	**10**		√		

Table 2

Comparison of different kinetics models for the striatal binding of PET tracer [^{18}F]VAT

Methods Parameters	Modeling with arterial blood input function (mean ± SD, n = 3)				Reference based modeling (mean ± SD, n = 7)		
	2TCM	LoganAIF	1TCM	MA1	RTM	SRTM	LoganREF
K_1 (mL·cm^{-3}·min^{-1})	0.113 ± 0.068 (35%) *	NA **	0.221 ± 0.20 (52%)	NA	(*** $R_1 = K_1/K_1'$ 0.847 ± 0.08 (4%))	(*** $R_1 = K_1/K_1'$ 0.84 ± 0.023 (1%))	NA
k_2 (min^{-1})	0.027 ± 0.005 (11%)	NA	0.009 ± 0.004 (26%)	NA	0.17 ± 0.16 (36%)	0.032 ± 0.007 (8%)	NA
k_3 (min^{-1})	0.019 ± 0.009 (27%)	NA	NA	NA	0.05 ± 0.04 (30%)	NA	NA
k_4 (min^{-1})	0.005 ± 0.001 (12%)	NA	NA	NA	0.025 ± 0.02 (30%)	NA	NA
V_T (mL· cm^{-3})	22.31 ± 20.7 (54%)	16.87 ± 17 (58%)	22.12 ± 14.1 (37%)	21.45 ± 14 (38%)	NA	NA	NA
DVR	4.37 ± 0.34 (4%)	3.58 ± 0.9 (15%)	3.70 ± 1.1 (17%)	3.17 ± 1 (18%)	3.11 ± 0.46 (6%)	3.15 ± 0.46 (6%)	3.11 ± 0.43 (5%)
BP_{ND}	3.37 ± 0.34 (6%)	2.58 ± 0.9 (20%)	2.69 ± 1.1 (24%)	2.17 ± 1 (27%)	2.11 ± 0.46 (8%)	2.15 ± 0.46 (8%)	2.11 ± 0.43 (8%)
MSC	2.44 ± 1.3	3.30 ± 0.2	2.13 ± 1.1	1.51 ± 0.7	6.19 ± 0.09	5.75 ± 0.49	4.64 ± 1.2
χ^2	0.148 ± 0.09	0.003 ± 0.0002	0.41 ± 0.16	0.62 ± 0.3	0.082 ± 0.01	0.055 ± 0.044	0.002 ± 0.001
F-test (p value)	0.35 ± 0.21	0.79 ± 0.006	0.40 ± 0.34	0.045 ± 0.03	0.95 ± 0.02	0.91 ± 0.09	0.84 ± 0.12

* The values in the parentheses indicate the relative standard error (rSE) for each estimate

** NA: not applicable

*** No K_1 values

Table 3

Kinetics modeling results by 2TCM (mean ± SD, n = 3)

ROI	K_1 (mL·cm^{-3}·min^{-1})	k_2 (min^{-1})	k_3 (min^{-1})	k_4 (min^{-1})	V_T (mL· cm^{-3})	k_3 / k_4	BP_{ND} = DVR-1	MSC	χ^2	F-test p-value
Striatum	0.113 ± 0.068	0.027 ± 0.005	0.019 ± 0.009	0.005 ± 0.001	22.31 ± 20.71	3.52 ± 1.14	3.37 ± 0.34	2.44 ± 1.27	0.17 ± 0.07	0.32 ± 0.25
rSE *, %	35	11	27	12	54	19	6			
Thalamus	0.112 ± 0.061	0.030 ± 0.004	0.006 ± 0.002	0.004 ± 0.001	10.09 ± 8.25	1.38 ± 0.26	1.16 ± 0.24	2.81 ± 0.61	0.22 ± 0.07	0.70 ± 0.01
rSE, %	31	8	19	14	47	11	12			
Hippocampus	0.102 ± 0.059	0.035 ± 0.008	0.014 ± 0.010	0.014 ± 0.013	7.46 ± 5.56	1.15 ± 0.62	0.61 ± 0.41	2.79 ± 0.28	0.21 ± 0.09	0.69 ± 0.11
rSE, %	33	13	41	54	43	31	39			
Frontal cortex	0.103 ± 0.046	0.035 ± 0.004	0.010 ± 0.012	0.004 ± 0.001	7.13 ± 6.52	0.94 ± 0.64	0.44 ± 0.10	2.59 ± 0.95	0.29 ± 0.06	0.69 ± 0.07
rSE, %	26	7	69	14	53	39	13			
Vermis	0.180 ± 0.069	0.068 ± 0.005	0.004 ± 0.003	0.005 ± 0.001	4.77 ± 2.72	0.75 ± 0.43	0.22 ± 0.55	3.82 ± 0.12	0.23 ± 0.05	0.92 ± 0.05
rSE, %	22	4	43	12	33	33	144			
White matter	0.065 ± 0.041	0.026 ± 0.005	0.006 ± 0.002	0.006 ± 0.001	5.66 ± 4.49	1.01 ± 0.32	0.21 ± 0.13	2.93 ± 0.72	0.15 ± 0.04	0.63 ± 0.13
rSE, %	36	11	19	10	46	18	36			
Midbrain	0.107 ± 0.091	0.039 ± 0.009	0.007 ± 0.003	0.006 ± 0.001	5.61 ± 4.55	1.06 ± 0.30	0.18 ± 0.13	2.26 ± 0.74	0.23 ± 0.04	0.58 ± 0.12
rSE, %	49	13	25	10	47	16	42			
Occipital cortex	0.101 ± 0.054	0.039 ± 0.005	0.004 ± 0.001	0.005 ± 0.001	5.51 ± 4.97	0.82 ± 0.53	0.12 ± 0.075	3.26 ± 0.21	0.18 ± 0.05	0.79 ± 0.05
rSE, %	31	7	14	12	52	37	36			
Temporal cortex	0.086 ± 0.042	0.033 ± 0.003	0.003 ± 0.001	0.005 ± 0.002	5.23 ± 4.45	0.74 ± 0.48	0.097 ± 0.076	3.01 ± 0.58	0.18 ± 0.05	0.72 ± 0.02
rSE, %	28	5	19	23	49	37	45			
Cerebellum- Hemispheres	0.144 ± 0.093	0.063 ± 0.010	0.007 ± 0.005	0.004 ± 0.003	5.85 ± 5.88	1.09 ± 0.84	0.00 ± 0.00	2.50 ± 0.48	0.52 ± 0.33	0.62 ± 0.41
rSE, %	37	9	41	43	58	0.45	NA **			

* rSE: relative standard error

** NA: not applicable

Table 4

Summary of kinetics modeling results based on reference (cerebellum- hemispheres) based methods (mean ± SD, n = 7)

ROI	LoganREF	SRTM		
	BP_{ND}	BP_{ND}	R_1	k_2 (min^{-1})
Striatum	2.11 ± 0.4	2.15 ± 0.5	0.85 ± 0.1	0.032 ± 0.01
Thalamus	0.76 ± 0.3	0.79 ± 0.3	0.95 ± 0.2	0.059 ± 0.02
Hippocampus	0.47 ± 0.3	0.48 ± 0.2	0.79 ± 0.1	0.053 ± 0.04
Frontal cortex	0.29 ± 0.2	0.32 ± 0.2	0.82 ± 0.3	0.055 ± 0.02
White matter	0.17 ± 0.2	0.17 ± 0.2	0.47 ± 0.1	0.032 ± 0.01
Middle brain	0.15 ± 0.2	0.17 ± 0.1	0.74 ± 0.2	0.066 ± 0.1
Occipital cortex	0.13 ± 0.1	0.12 ± 0.1	0.81 ± 0.3	0.053 ± 0.02
Temporal cortex	0.11 ± 0.1	0.10 ± 0.08	0.63 ± 0.2	0.074 ± 0.07
Vermis	0.063 ± 0.2	0.081 ± 0.07	1.08 ± 0.4	0.064 ± 0.6

Table 5

Striatal BP_{ND} estimates of [^{18}F]VAT using different scan duration (mean ± SD, n = 7)

Scan duration for analysis	120 min	90 min	60 min	45 min
LoganREF *	2.11 ± 0.43	1.86 ± 0.45	1.69 ± 0.49	1.60 ± 0.58
SRTM	2.15 ± 0.46	2.18 ± 0.37	2.14 ± 0.49	2.67 ± 1.14

* LoganREF analysis uses data starting from 20 min post tracer injection.

Table 6

Table 6A Correlation (Pearson's coefficients, r) with different modeling methods for the estimation of BP_{ND}

r - value	2TCM	1TCM	MA1	LoganAIF	RTM	SRTM	LoganREF
2TCM		0.837	0.793	0.859	0.940	0.958	0.932
1TCM	0.837		0.995	0.997	0.954	0.950	0.943
MA1	0.793	0.995		0.989	0.915	0.873	0.887
LoganAIF	0.859	0.997	0.989		0.964	0.943	0.946
RTM	0.940	0.954	0.915	0.964		0.991	0.981
SRTM	0.958	0.950	0.873	0.943	0.991		0.994
LoganREF	0.932	0.943	0.887	0.946	0.981	0.994	

Table 6B Correlation (p-values) with different modeling methods for the estimation of BP_{ND}

p - value	2TCM	1TCM	MA1	LoganAIF	RTM	SRTM	LoganREF
2TCM		0.082	0.104	0.071	**0.030**	**0.021**	**0.034**
1TCM	0.082		0.003	0.002	0.023	0.025	0.029
MA1	0.104	0.003		0.006	0.042	0.064	0.056
LoganAIF	0.071	0.002	0.006		0.018	0.029	0.027
RTM	**0.030**	0.023	0.042	0.018		0.005	0.009
SRTM	**0.021**	0.025	0.064	0.029	0.005		0.003
LoganREF	**0.034**	0.029	0.056	0.027	0.009	0.003	

Table 7

Table 7A Test-retest variability (TRV) and intraclass correlation coefficient (ICC) from LoganREF modeling (Mean ± SD from 3 NHP subjects)

ROIs	test	retest	TRV%	t test p-value	ICC
	BP_{ND}	BP_{ND}	(% ± SD)		
Striatum	2.39 ± 0.73	2.26 ± 0.46	7.91 ± 0.67	0.42	0.92
Thalamus	0.70 ± 0.10	0.74 ± 0.09	4.99 ± 0.09	0.34	0.93
Hippocampus	0.46 ± 0.18	0.47 ± 0.19	0.95 ± 0.17	0.49	0.99
Frontal cortex	0.29 ± 0.06	0.29 ± 0.08	4.65 ± 0.06	0.48	0.98

Table 7B Test-retest variability (TRV) and intraclass correlation coefficient (ICC) from SRTM modeling (Mean ± SD from 3 NHP subjects)

ROIs	test	retest	TRV%	t test p-value	ICC
	BP_{ND}	BP_{ND}	(% ± SD)		
Striatum	2.38 ± 0.69	2.15 ± 0.38	8.38 ± 0.62	0.35	0.83
Thalamus	0.77 ± 0.13	0.77 ± 0.12	0.36 ± 0.11	0.49	0.99
Hippocampus	0.46 ± 0.16	0.48 ± 0.14	4.47 ± 0.13	0.49	0.99
Frontal cortex	0.32 ± 0.07	0.30 ± 0.03	8.64 ± 0.05	0.37	0.72